PNAS RESEARCH ARTICLE | ENGINEERING

Toward the development of plasticity theories for application to small-scale metal structures

Bin Zhang[a,1], K. L. Nielsen[b,1], J. W. Hutchinson[c,2], and W. J. Meng[a,2]

Contributed by J. W. Hutchinson; received July 29, 2023; accepted September 19, 2023; reviewed by Huajian Gao and Peter Gudmundson

Experiments are performed on micron-scale single-crystal prototypical structural elements experiencing combined torsion and bending to gather data on their load-carrying capacity in the range of size and strain relevant to micron-scale structures for which little data are available. The observed strengthening dependence on size for the structural elements is in general accord with trends inferred from prior tests such as indentation and pure torsion. In addition, the experiments systematically reveal the strengthening size-dependence of structural elements whose surface has been passivated by a very thin Cr coating, an effect shown to have substantial strengthening potential. A state-of-the-art strain gradient plasticity theory is used to analyze the structural elements over the entire range of size and loading. While the computed trends replicate the experimental trends with reasonable fidelity, the predictive exercise, which is representative of those that will be required in micron-scale structural analysis, brings to light constitutive and computational issues which will have to be addressed before micron-scale plasticity theory can serve as effectively at the micron scale as conventional plasticity does at larger scales.

structures | plasticity | micron scale

Significance

Modern engineering encompasses control of material structure, composition, and architecture. Advanced fabrication technologies enable increasingly small architectural designs, from millimeter to submicron length scales. Conventional plasticity theory, mature for macroscale applications, no longer describes the deformation behavior of such small-scale metal structures. We conduct experiments on prototypical micron-scale structural elements, measuring quantitatively their deformation behavior over relevant ranges of size and strain and its dependence on surface conditions. A state-of-the-art micron-scale plasticity theory is used to analyze these structural elements and largely captures the experimental trends. The combined experimentation-modeling effort highlights constitutive and computational issues that will have to be addressed before micron-scale plasticity theory can serve as effectively as conventional plasticity does at the macroscale.

Plastic deformation at small length scales has been studied intensely since the demonstration that flow stress depends not only on the plastic strain but also on the gradient of plastic strain (1). As the external specimen dimension decreases to the micron range, flow stress is also observed to increase with decreasing size in the absence of a strain gradient (2), when deformation becomes dominated by dislocation nucleation rather than dislocation interaction (3). The influence of strain gradients on plastic deformation is not only apparent in specialized experiments, e.g., nano/microindentation (4) and microbending of foils (5), but also manifests in microscale metal manufacturing technology applications, including molding (6, 7), extrusion (8, 9), wire drawing (10), and rolling (11). Furthermore, recent modeling work suggests that strain gradient effects enhance the resistance to plastic buckling of columns as the characteristic column dimension approaches the micron scale (12).

These findings suggest that plastic strain gradient effects must also affect the structural response of cellular metals. Upon global loading, the structural members within the cellular metal are subjected to various modes of deformation: tension, compression, bending, torsion, and their combinations. Cellular metals have been studied for several decades (13). While early production methods produce metal foams with a random cellular architecture and typical cell sizes in the 1 to 10 mm range (14), more recent activities leverage various additive manufacturing (AM) technologies to produce ordered cellular architectures with beam-, plate-, and minimal surface- based topologies. Global deformation of such mechanical metamaterials, i.e., materials composed of such purposefully designed microarchitectures, elicits a structure-like response (15). In such metamaterials, the characteristic cell sizes range from the mm scale down to the micron scale and the characteristic dimension of individual structural members goes down to the micron and submicron ranges (16). When such metal metamaterials are subjected to global compression loading, almost complete recovery from large effective compression strains has been demonstrated (17). The significant extent of recovery of such lattice structures after loading has been attributed to limited plastic deformation of the individual structural members under load despite the large global deformation (17). While previous indentation studies on nanoscale Ni lattice structures synthesized through a hybrid self-assembly technique revealed a significant size effect (18), investigations along these lines have been limited in number, and the potential for such ordered cellular metal structures to exhibit abnormal strength-to-weight ratios remains to be explored fully. In addition, altering the surface condition of the structural members is expected to modify the overall mechanical response, as the condition of the surface can influence dislocation activities within the bulk. A satisfactory theory for such small-scale mechanical structures should be able to provide a uniformly faithful description of materials' mechanical response under the various modes of deformation or their combinations, including effects of surface modification which is

Author contributions: K.L.N., J.W.H., and W.J.M. designed research; B.Z., K.L.N., and W.J.M. performed research; B.Z., K.L.N., J.W.H., and W.J.M. analyzed data; and B.Z., K.L.N., J.W.H., and W.J.M. wrote the paper.

Reviewers: H.G., Nanyang Technological University; and P.G., Kungliga Tekniska Högskolan (KTH Royal Institute of Technology).

The authors declare no competing interest.

[1]B.Z. and K.L.N. contributed equally to this work.

[2]To whom correspondence may be addressed. Email: jhutchin@fas.harvard.edu or wmeng1@lsu.edu.

This article contains supporting information online at https://www.pnas.org/lookup/suppl/doi:10.1073/pnas.2312538120/-/DCSupplemental.

Published October 23, 2023.

expected to exert an increasingly significant influence on the overall mechanical behavior as the characteristic dimension of the structural members approaches the micron scale.

Intense efforts have been devoted to developing plasticity models that consider the effect of size explicitly. Geometrically necessary dislocations (GNDs) are known to appear in regions with large plastic strain gradients to accommodate the lattice curvature (19–21). The local stress fields near such GNDs lead to higher free energies and additional dissipation associated with dislocation motion, giving rise to size effects in inhomogeneous plastic deformation. Existing strain gradient plasticity (SGP) models have been formulated for polycrystals and single crystals using a mix of continuum mechanics phenomenology and dislocation physics (22–31). The constitutive relations in such models contain at least one explicit length scale parameter, with a typical value in the range between ~0.1 and ~10 μm which must be calibrated for each material (32). However, a unique length parameter is often not sufficient to fit experimental datasets from different loading scenarios, and it has been speculated that either the length scale parameter evolves as plastic deformation proceeds (33) or the experiments display combined microstructure and strain gradient effects (34). Despite these uncertainties, such SGP theories are believed to be the best candidates for predicting outcomes of experiments involving micron-scale plastic deformation with significant strain gradients. However, for SGP theory to mature to a reliable level for modeling small-scale structures, as conventional continuum plasticity has matured to the point of being able to predict outcomes of macroscale plasticity experiments, it is imperative to have meaningful comparisons between experimental data and model predictions in the relevant length scale range: from the microscale (e.g., 1 to 10 μm) to the mesoscale (e.g., 10 to 100 μm). To simplify data interpretation and comparison with models, it is desirable to perform meso- to microscale mechanical testing in which the imposed deformation geometries are sufficiently simple yet with well-defined and significant strain gradients.

Meso/microscale torsion is such a basic test. The deformation geometry is simple yet possesses a definite strain gradient. Since the work by Fleck et al. (1), additional torsional loading on polycrystalline Cu wires was performed by Dunstan et al. with diameters of 50 μm and 10 μm (35, 36), by Liu et al. with diameters ranging from 105 μm to 18 μm (37, 38), and by Lu and Song with diameters ranging from 180 μm to 16 μm (39). While Dunstan et al. (35, 36) and Liu et al. (37, 38) observed relatively moderate size effects in the torsional response, Lu and Song did not observe any size effect in their measured torsional response (39). Relative to the abundant reports in the literature on instrumented nano/microindentation (40) and nano/micropillar compression (3), the number of microtorsion tests reported in the literature is scarce, and the agreement between data is worse. This scarcity of data in microtorsion can be attributed to the fact that, up to this point, different investigators essentially adopted the same torsional testing protocol, which represents a scaled-down version of a macroscopic test. This protocol suffers from a lack of torque resolution (41), as well as difficulties in wire specimen preparation, characterization, and surface treatment. In all the reported microtorsion experiments, tested wire diameters have never been less than 10 μm, and loading of single-crystal wires has never been performed. The observed size effects from polycrystalline wires may also reflect an interplay between grain size influence and strain gradient hardening.

The present work describes a micro/mesoscale testing protocol that elicits a combined torsion/bending response from the tested material volume. Our alternate protocol leverages well-established capabilities for precision nano/micro/mesoscale machining with focused ion beam and precision instrumented compression loading. This test protocol can be applied to polycrystal as well as single-crystal specimens with equal ease. Following this protocol, we have achieved reliable measurements of torsion/bending response at characteristic specimen sizes from ~30 μm down to ~2 μm on single-crystal Cu specimens. We also demonstrate modification of specimen surface conditions through vapor phase thin film deposition, and the significant effect such surface passivation has on measured torsion/bending response for micron-scale structures. Finite element method (FEM) simulations of the load-deflection response of the test specimens are compared with a wide range of experimental data, with and without surface passivation. The FEM simulations employ one of the most widely used SGP constitutive models. In choosing this model, we have had to confront unresolved issues surrounding currently available SGP models. These issues will be highlighted in our discussion with the aim of helping to focus future research efforts to advance the utility of the theory.

Torsion/Bending Experiments of a Micron Scale Structural Element

Instead of performing wire torsion following protocols described in refs. 1 and 35–39, we devised an alternate "L-beam" protocol and conducted testing in-situ a scanning electron microscope (SEM). The L-beam can be regarded as a structural element supporting a load that generates both twisting and bending. The design of the L-beam torsion/bending test is illustrated in Fig. 1. Fig. 1*A* shows a 52° tilted view of one as-machined specimen: a suspended beam shaped like an "L" with a square cross-section. Deformation of the torsion arm is achieved through a downward compression loading near the end of the load arm by a flat-ended punch. The L-beam specimen was machined by Xe plasma focused ion beam (PFIB) from a 5 mm × 5 mm × 1 mm Cu single crystal, with the top surface normal parallel to Cu [111]. The normals of the top and front surfaces of the square torsion arm are parallel, respectively, to the Cu [111] and $[1\bar{1}0]$ directions. For the L-beam shown in Fig. 1*A*, the torsion arm width w and half-width a with $w = 2a$, height h, and length l are proportioned to be $l = 2w = 2h$. The load arm shares the same width and height as the torsion arm, and its total length l_2 is $4w$. The values of w, h, l, and l_2 for the specimen shown in Fig. 1*A* are, respectively, 4.8 μm, 4.8 μm, 10.3 μm, and 19.8 μm. Fig. 1*B* shows a 0° plan view of another as-machined <111> Cu L-beam, with w, h, l, and l_2 being, respectively, 19 μm, 18.6 μm, 38.8 μm, and 75.6 μm. The load length l_L, measured from the center of the torsion arm to the load point, is slightly less than 60 μm. Fig. 1*C* shows one still frame from a video file, illustrating the compression load by a flat punch at the end of the load arm. The entire loading process and the associated deformation of one L-beam specimen were recorded in a video file, and presented in *SI Appendix*, section S1 and Movie S1.

Fig. 2 documents the deformation morphology of and defect development within <111> Cu L-beam specimens with no additional surface modification after PFIB fabrication. Fig. 2 *A* and *B* show, respectively, the top view of one L-beam with w ~4.5 μm, before and after deformation. The straight-line marks left by the Xe^+ beam during the machining process are clearly visible in Fig. 2*A*. Fig. 2*B* shows that, after deformation, the straight-line marks became distorted out of the original plane into S-shapes, consistent with expectations from the elastic solution for torsion of a square beam (42). Fig. 2*C* shows the front view of another L-beam with w ~20 μm after deformation, in which the deformation of the torsion arm is clearly visible. The mark on the load arm, highlighted by the red arrow, resulted

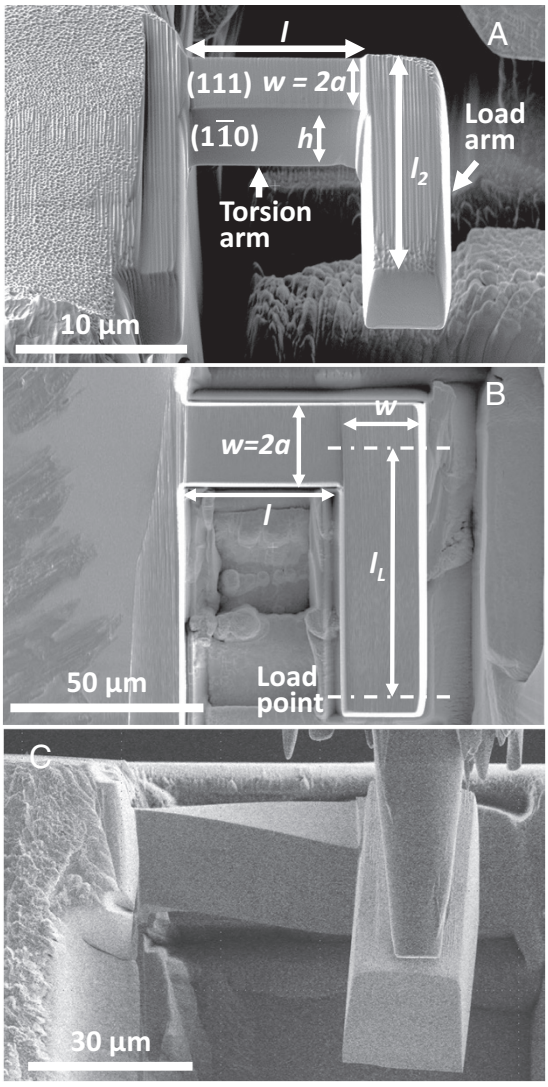

Fig. 1. Design of the L-beam torsion/bending test: (*A*) a 52° tilted view of one as-machined single crystal <111> Cu L-beam. The top and front surfaces of the square torsion arm are, respectively, Cu (111) and (1$\bar{1}$ 0). The torsion arm width *w*, height *h*, and length *l* are, respectively, 4.8 μm, 4.8 μm, and 10.3 μm. The load arm total length l_2 is 19.8 μm; (*B*) a 0° plan view of another as-machined <111> Cu L-beam with *w*, *h*, *l*, and l_2 being, respectively, 19 μm, 18.6 μm, 38.8 μm, and 75.6 μm. The load length l_L is slightly less than 60 μm; (*C*) one frame of a video file showing the compression loading at the end of the load arm by a flat-ended punch. The torsion arm half-width is *a*, with *w* = 2*a*.

from contact with the flat punch during compression loading and served as a convenient marker for measuring the load length l_L. Fig. 2*D* shows a higher magnification view of the front surface of the deformed L-beam shown in Fig. 2*C*. The red arrows highlight deformation-induced surface slip steps, the presence of which clearly indicates slip activation within the deformed single-crystal specimen. Fig. 2 *E* and *F* show, respectively, views of the front and back surfaces of one deformed L-beam with *w* ~20 μm. Fig. 2*E* again shows that originally straight ion beam marks on the beam front surface have been distorted out-of-plane into S-shapes. Three distinct groups of surface slip steps are present due to the deformation, highlighted by short-dashed lines of red, green, and blue colors, signifying dislocation activities on at least three distinct {111} slip planes. Similar deformation morphologies are consistently observed on deformed single-crystal Cu L-beams of different sizes. In addition to the distinct groups of surface slip steps, residual defects are retained within the interior of deformed L-beams. Transmission electron microscopy (TEM) was used to examine the longitudinal cross-section of deformed L-beam specimens, with the TEM lamella parallel to the L-beam front surface. Further details on TEM specimen fabrication are presented in *SI Appendix*, section S2 and Fig. S1. Fig. 2*G* shows a low-magnification TEM bright field (BF) image from the bottom region of one deformed <111> Cu L-beam. Extensive twins and stacking faults formed close to the bottom L-beam surface. The *Inset* shows a [1$\bar{1}$0] zone axis electron selected area diffraction (SAD) pattern from the twinned region shown in Fig. 2*G* in which twin diffraction spots are clearly present. Fig. 2*H* shows a high-resolution phase contrast image obtained from the same region, in which the deformation-induced twinning is evident.

Two series of <111> Cu L-beam specimens of varying sizes, with orientations identical to that shown in Fig. 1, were fabricated by PFIB machining. For these specimens, no additional surface modification was performed, and slip steps were present on these unpassivated surfaces of the deformed specimens, as illustrated in Fig. 2. In the first series, the dimensions of the torsion arm and load arm were kept, respectively, at $l = 2w = 2h$ and $l_2 = 4w = 4h$ (dubbed "2 × 4" L-beams). The second series have relatively longer load arms, with $l = 2w = 2h$ and $l_2 = 6w = 6h$ (dubbed "2 × 6" L-beams). In the present experiments, the beam half-width *a* ranged from ~15 μm to ~1 μm, and the beam width $w = 2a$ ranged from ~30 μm to ~2 μm. Measured mechanical response from L-beam loading consists of a continuous record of the compression load *F* vs. the punch displacement *d*. The torsion arm is subjected to a torque, $T = F \times l_L$. The torsional angle θ is related to the punch displacement, $\tan(\theta) = d/l_L$. To capture the elastoplastic response of the deformed L-beams, the measured raw data are plotted in the same scaled form as that used by Fleck et al. (1), that is

$$F l_L/a^3 \text{ vs. } \left(d/l_L\right)(a/l). \qquad [1]$$

The significance of this scaling, which is pertinent to this study, is that for self-similar L-beam specimens (i.e., having fixed dimension ratios), the relation of the force and deflection in Eq. **1** is independent of specimen size for any conventional plasticity theory having no dependence on a material length. Fig. 3*A* plots measured torsion/bending responses in the form of Eq. **1** for the series of 2 × 4 <111> Cu L-beam specimens with unpassivated surfaces. The range of the response is purposely chosen to be relevant to structural elements in architected cellular metals. The curves show an initial elastic section, with the scaled torque Fl_L/a^3 increasing rapidly with increasing $(d/l_L)(a/l)$, transitioning to a plastic regime in which Fl_L/a^3 increases much more slowly with increasing $(d/l_L)(a/l)$. Fig. 3*B* shows values of Fl_L/a^3 at $(d/l_L)(a/l) = 0.02$ vs. *a*, providing a strength measure of the transition from elasticity to plasticity analogous to that used in large-scale plasticity. These data show a significant size effect, with Fl_L/a^3 (which is independent of size according to conventional plasticity) increasing by a factor of ~3 as the torsion arm width *w* decreases from ~30 μm to ~2 μm. Fig. 3 *C* and *D* plot measured data for a corresponding series of 2 × 6 <111> Cu L-beams with unpassivated surfaces in the same manner as Fig. 3 *A* and *B*. At the same beam dimension *a* (e.g., data points at *a* ~4 μm), the value of Fl_L/a^3 is about 10 to 20% lower for the 2 × 6 L-beams. The different sets of load arm lengths in 2 × 4 and 2 × 6 <111> Cu L-beams led to different interactions between bending and torsion and consequently the difference in measured mechanical responses. Such interaction between bending and torsion is not uncommon in structural elements.

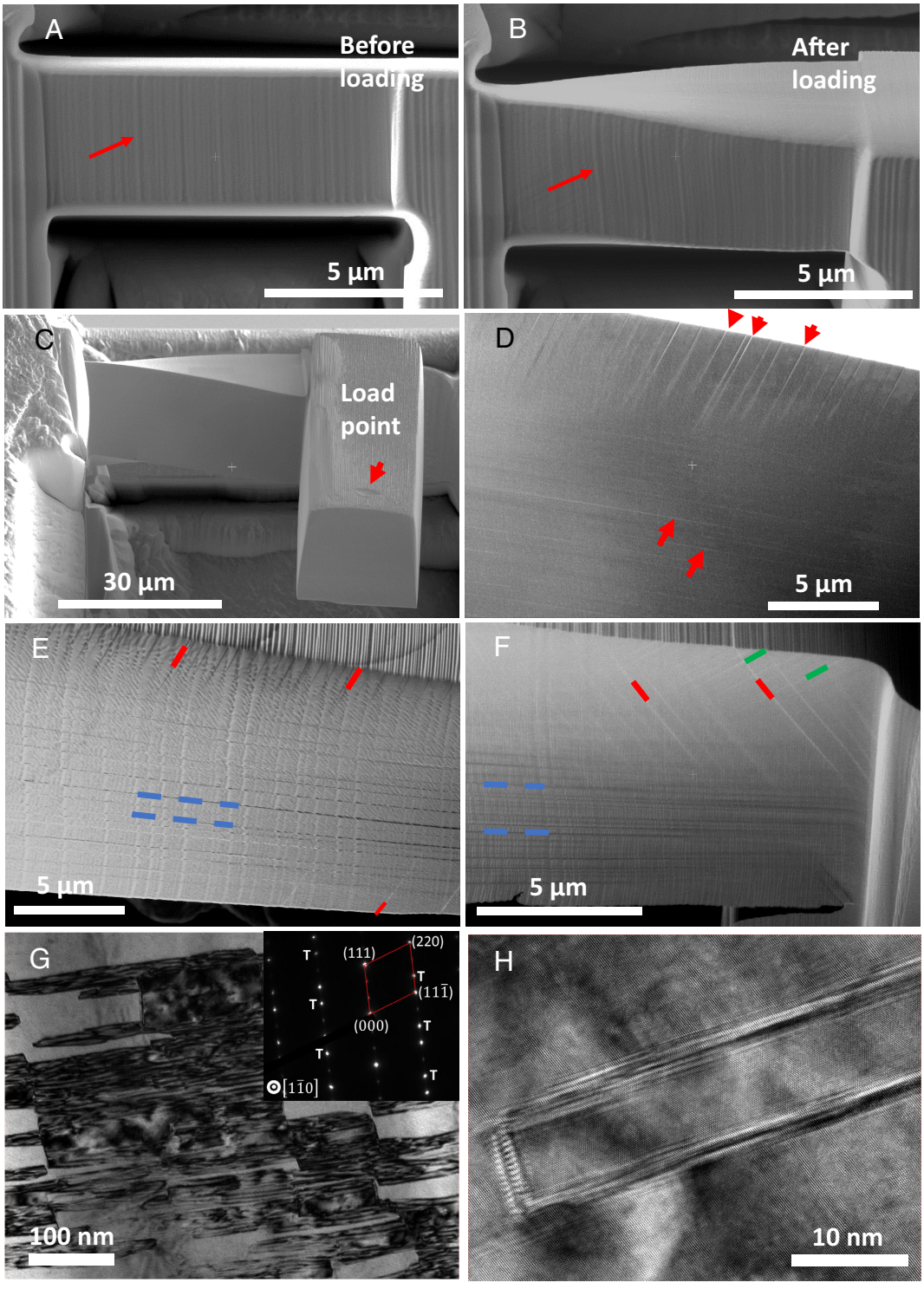

Fig. 2. Morphology of and defect development within deformed <111> Cu L-beams with unpassivated surfaces: (*A* and *B*) top view of one L-beam with w ~ 4.5 μm before and after deformation. The red arrows highlight the straight marks left during Xe^+ ion milling and how they deform after loading; (*C*) front view of another L-beam with w ~ 20 μm after deformation; the red arrow highlights the mark on the load arm made by the flat punch during loading; (*D*) a higher magnification view of the front surface of the deformed L-beam shown in (*C*). The red arrows highlight the deformation-induced surface slip steps; (*E* and *F*) front and back surface view of one L-beam with w ~ 20 μm. Short dashed lines of different colors (red, blue, and green) highlight surface slip steps due to dislocation activities on three distinct groups of Cu {111} slip planes; (*G*) a longitudinal cross-section TEM BF image of the twinned region near the bottom of one deformed <111> Cu L-beam. The *Inset* shows an SAD pattern from the twinned region. Twin diffraction spots are marked by T; (*H*) a high-resolution phase contrast image showing deformation-induced twinning.

Simulations with SGP

To extract material properties from the load-displacement data of almost any test specimen requires an analysis of the test and, when plasticity occurs, the adoption of an elastic-plastic constitutive model. Similarly, given a constitutive model and material properties, the prediction of the behavior of a structural element subject to a specific loading history requires an analysis of the structure/load combination. The geometry of the L-beam specimen leaves little choice for such analyses other than the

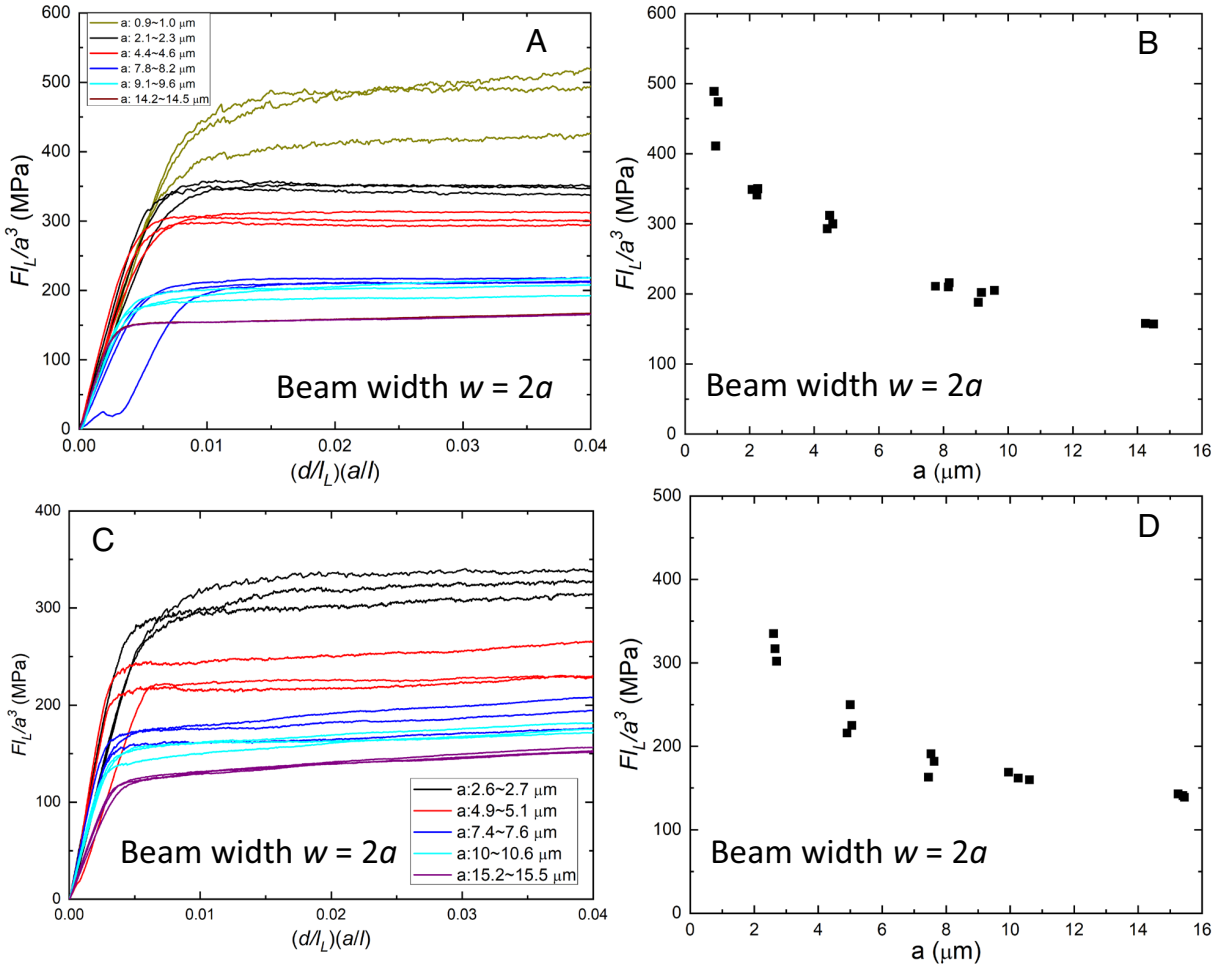

Fig. 3. Measured mechanical response from tests on L-beams with unpassivated surfaces: (*A*) Fl_L/a^3 vs. $(d/l_L)(a/l)$ for a series of 2 × 4 <111> Cu L-beams with torsion arm half-width a ranging from ~14 μm to ~1 μm; (*B*) value of Fl_L/a^3 at $(d/l_L)(a/l) = 0.02$ vs. a; (*C*) Fl_L/a^3 vs. $(d/l_L)(a/l)$ for a series of 2 × 6 <111> Cu L-beams with torsion arm half-width a ranging from ~15 μm to ~2 μm; (*D*) value of Fl_L/a^3 at $(d/l_L)(a/l) = 0.02$ vs. a.

use of three-dimensional (3D) FEMs, for which computational codes are well-developed and commercially available for conventional plasticity but not for SGP. The computations analyzing the present L-beam specimen tests were performed using a noncommercial 3D isotropic SGP FEM code based on the work by Nielsen and Niordson (43). Before describing the results, however, we believe that it is important to discuss several points related to the present status of SGP constitutive models and their implementation in FEM codes. Progress in the plasticity of small-scale structures hinges on advancing both the constitutive models and computational capabilities.

(i) The present L-beam specimens are fabricated from an face-centered cubic single-crystal of Cu. At present, no 3D FEM codes for single-crystal SGP are available for either small or large strain applications. In the absence of such single-crystal SGP codes and knowing that deformation of the L-beam specimens induces slip on multiple crystallographic slip systems (see, e.g., Fig. 2), we employed an FEM code based on an isotropic SGP constitutive model to render a reasonable approximation of the behavior of the present single-crystal structures under load and calibrated it to data from selected single-crystal L-beam specimens. A severe check on the fidelity of the calibrated model is provided by using it to predict the behaviors of L-beam specimens with and without surface passivation, as this involves only constraints on plasticity at the specimen surfaces and no change in material parameters.

(ii) SGP constitutive models for single crystals have been developed with a mathematical structure that ensures that plastic dissipation is non-negative, similar to the construction of the isotropic SGP model used in this paper. For applications such as the present case with monotonic loading and no abrupt changes in the loading direction, i.e., nearly proportional loading, these models have proven to be physically sound and reliable. However, for applications in which the direction of loading or deformation changes abruptly, referred to as nonproportional loading, this class of theories for both isotropic and single-crystal SGP produce unsound predictions in the form of an elastic incremental response when a plasticity should occur (44). A theory of the type used in this paper would significantly underestimate the contribution of plasticity in each case in the vicinity of the load transition. Physically sound constitutive alternatives exist for both isotropic and single-crystal SGP models (45, 46), but they have not yet been validated against experiments.

The comments above illustrate two of the outstanding issues to be resolved before plasticity theories capable of providing reliable deformation and strength analyses of any small-scale structures

will be available to the technological community, analogous to the roles played by J_2 flow theory and conventional single-crystal plasticity for large-scale applications. In this paper, the second issue regarding strongly nonproportional loading is not a concern. However, using an isotropic formulation of SGP to model a structure fabricated from a single crystal clearly highlights the development of 3D single-crystal SGP codes as a priority.

The gradient-enriched isotropic plasticity theory by Gudmundson (24) and Fleck and Willis (27, 28) is adopted to simulate the L-beam experimental results. The elastic behavior is characterized by Young's modulus, $E = 120$ GPa, and Poisson's ratio, $\nu = 0.33$, of isotropic polycrystalline Cu. The plastic behavior is specified by a standard form for the tensile stress-strain curve in the large-scale limit, $\sigma = \sigma_Y\left(1 + k\varepsilon_P{}^N\right)$, with ε_P as the plastic strain, σ_Y as the initial yield stress, N as the strain hardening exponent and k as a fitting constant, and one additional material length parameter, l_D, scaling the plastic strain gradients. When the product of l_D and the plastic strain gradients is small, this theory reduces to the J_2 flow theory, the conventional plasticity workhorse. We first evaluated σ_Y, N, and k by fitting the simulation output to the data from the unpassivated 2 × 4 L-beam specimen with a ~14 μm. Then, l_D was evaluated by fitting the simulation output to the data from the unpassivated 2 × 4 L-beam specimen with a ~2 μm. Further details of the constitutive model are provided in the *Materials and Methods* section, with the values of the material parameters used in the simulations given in Table 1.

Fig. 4 *A* and *B* plot, respectively, measured response together with the corresponding SGP FEM simulation outputs for the unpassivated 2 × 4 and 2 × 6 L-beams. Dimensions of the L-beams used in the FEM simulations are taken to be those measured from SEM imaging of the individual L-beam specimens used in the experiment. The same set of material parameters was used in the simulations for both the 2 × 4 and 2 × 6 L-beams. Fig. 4 *C* and *D* shows, respectively, measured and simulated values of Fl_L/a^3 as a function of a, taken at $(d/l_L)(a/l) = 0.02$, for the series of unpassivated 2 × 4 and 2 × 6 L-beams. At two different L-beam specimen geometries (2 × 4 vs. 2 × 6), the FEM simulation output matches the measured values rather faithfully over the entire range of beam dimensions. It is worth emphasizing that the load/displacement data in these tests fall in the range of interest for many important structural applications, namely the range in which plastic yielding first occurs and then develops to the extent that the plastic strains become larger than the elastic strains but still relatively small. Some of the early torsion tests, such as those in Fleck et al. (1), generate data in the range where the plastic strains are, by comparison, large, on the order of unity, with little resolution of behavior at and immediately subsequent to yield.

Effects of Surface Passivation

Dislocation activities are expected to initiate from external surfaces of a torsionally loaded specimen since the maximum shear stress occurs there. The configuration of the L-beam specimen thus offers an especially good opportunity to study the effect of surface passivation on the mechanical response. Deposition of thin metal coatings is known to alter the occurrence of surface intrusions/extrusions, thus influencing the specimen fatigue limit during cyclic loading (47). An example is thin coatings of Cr deposited onto stainless steel substrates, which have been shown to possess a relatively high hardness and impact the substrate fatigue life (48). Fig. 5 shows an example of surface passivation of one <111> Cu L-beam specimen, with w = 20 μm, through vapor phase deposition of a thin Cr coating. Fig. 5 *A* and *B* show, respectively, Cu K and Cr K energy dispersive spectroscopy (EDS) maps of the Cu L-beam after deposition of a thin Cr coating layer. The Cr coating thickness is sufficiently small such that Cu K X-ray is not significantly attenuated, leading to the uniform Cu K X-ray intensity shown in the EDS map of Fig. 5*A*. The uniform Cr K intensity shown in Fig. 5*B* indicates that a relatively uniform Cr coating layer has been deposited onto the top, front, and back surfaces of the Cu L-beam specimen. Due to the directionality of the vapor deposition flux, the L-beam bottom surface is not expected to be coated. Fig. 5*C* shows a FIB cross-section of the Cr coating on the L-beam specimen. A uniform coating layer is evident, the thickness of which is ~120 nm. Fig. 5*D* shows a low-magnification top view of the Cr-coated L-beam after deformation. A higher magnification view of the L-beam top surface subregion outlined in the red square is shown in Fig. 5*E*. Fig. 5*F* shows another higher magnification view of the L-beam front surface. Cracks formed in the Cr coating due to deformation, as highlighted, respectively, by the white and black arrows in Fig. 5 *E* and *F*. However, the extensive slip steps observed on uncoated L-beam specimens, shown in Fig. 2, are largely absent from the Cr-coated L-beam specimen. Observations shown in Fig. 5 indicate that a thin Cr coating is effective in blocking the formation of surface slip steps, and thus at least partially inhibiting dislocation activities at the specimen surface.

Table 1. Material parameters used in the SGP simulations

Parameter	Symbol	Value
Young's modulus (GPa)	E	120
Poisson's ratio	ν	0.33
Yield stress (MPa)	σ_Y	90
Strain hardening exponent	N	0.25
Strain hardening coefficient	k	0.045
Reference strain rate (s^{-1})	$\dot{\varepsilon}_0$	0.001
Strain rate sensitivity exponent	m	0.01
Length parameter (μm)	l_D	2

The difference between the mechanical response of <111> Cu L-beam specimens with and without surface passivation is shown in Fig. 6. Fig. 6 *A–D* plot measured values of Fl_L/a^3 vs. $(d/l_L)(a/l)$ for a series of 2 × 4 L-beam specimens with beam half-width a ranging between 14.2 to 14.5 μm, 9.0 to 9.6 μm, 4.4 to 4.6 μm, and 1.9 to 2.3 μm, respectively. The black and red lines denote, respectively, measured Fl_L/a^3 vs. $(d/l_L)(a/l)$ curves without and with the thin Cr coating. At the largest specimen size of a ~14.3 μm, the plastic yield point appears to be similar for both uncoated and coated L-beams, while the effective strain hardening rate of the Cr-coated L-beam appears to be significantly higher than that of the uncoated. In part, that increase reflects the fact that the coating is undergoing only elastic deformation and, while the coating contributes only a fraction of a percent to the overall load-carrying capacity prior to plastic yielding of the Cu, it makes a larger fractional contribution when the Cu becomes plastic. As the L-beam size decreases (e.g., a ~ 4.5 μm and 2.1 μm), the higher effective strain hardening rate for the Cr-coated L-beams persists while the apparent plastic yield point for the coated specimens increases with decreasing specimen size. The effect is large and roughly comparable to the increases due to the size effect in the absence of surface passivation.

Fig. 7*A* plots measured response of this series of surface passivated (Cr-coated) 2 × 4 Cu L-beams, together with the corresponding SGP FEM simulation outputs. With the same set of material parameters, the simulation outputs capture the trend of the

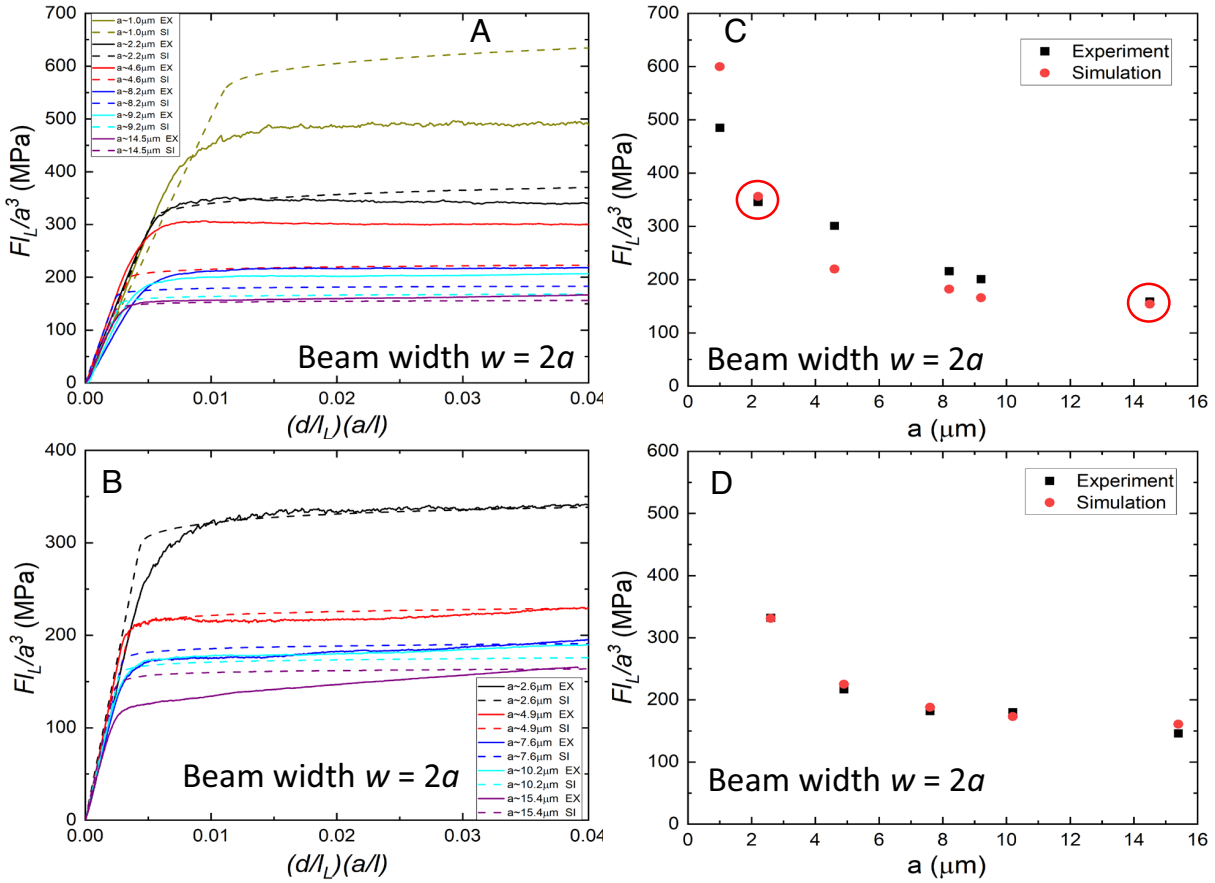

Fig. 4. Comparing L-beam data with SGP FEM simulations: (*A* and *B*) scaled torque vs. displacement for 2 × 4 and 2 × 6 L-beams with unpassivated surfaces at different beam half-width *a*. Dashed and solid lines represent, respectively, experimental data (EX) and SGP FEM simulation output (SI); (*C* and *D*) measured and computed values of the scaled torque Fl_L/a^3, taken at $(d/l_L)(a/l) = 0.02$, vs. *a*. The red circles in (*C*) highlight the two L-beam data points used to calibrate the material parameters in the SGP model.

experimental data reasonably well with a surface boundary condition change to enforce $\dot{\varepsilon}^p_{ij} = 0$ on the top, front, and back (but not the bottom) surfaces of the L-beam specimens. Strengthening due to passivation arises because the coating blocks dislocations as they approach the surface, thereby reducing local plastic flow and, more importantly, increasing the plastic strain gradients. Thus, the dominant effect of surface passivation can only be captured by a strain gradient formulation. Fig. 7*B* shows measured and simulated values of Fl_L/a^3 as a function of *a*, taken at $(d/l_L)(a/l) = 0.02$, for this series of surface passivated 2 × 4 Cu L-beams. Bearing in mind that no further model calibration is made, the experimental trends is well captured by the SGP FEM simulations, although the simulations for the larger specimens imply a larger increase in yield strength due to the coating than the experimental measurements reveal. For comparison, the corresponding experimental data for unpassivated 2 × 4 Cu L-beams are also displayed in Fig. 7*B*, illustrating again the significant difference in mechanical response brought about by changes in surface conditions as the characteristic specimen dimension decreases to the micron scale.

Specimen size effects in uniaxial pillar compression experiments have been well documented (2, 3), and a comparison between those and the presently studied L-beam deformation is warranted. Straight pillars with square cross-sections were fabricated from a 5 mm × 5 mm × 1 mm Cu single crystal, with the pillar top surface normal parallel to Cu [001]. Uniaxial compression was conducted in a displacement-controlled mode on <001> Cu square pillars with dimensions of ~2 μm × 2 μm × 6 μm, ~10 μm × 10 μm × 30 μm, and ~20 μm × 20 μm × 60 μm. Fig. 8 *A*–*C* show, respectively, typical morphologies of 2 μm, 10 μm, and 20 μm <001> Cu pillars deformed to an engineering strain ε of ~0.3. For the 2 μm and 10 μm pillars, deformation is dominated by strain bursts, clearly visible in Fig. 8 *A* and *B*. As is well documented, these strain bursts result from motion of dislocations after nucleation, which propagate along one particular {111} slip plane unimpeded until they reach the opposite side of the pillar, leading to rigid shears of one pillar portion with respect to another. As the pillar size increases to 20 μm, strain bursts are no longer observed and slip steps belonging to different Cu {111} planes appear on the pillar external surfaces as shown in Fig. 8*C*. Fig. 8*D* shows the nominal engineering compression stress σ plotted vs. ε for several 2 μm, 10 μm, and 20 μm pillars. The corresponding averaged σ value at $\varepsilon = 0.02$ is plotted vs. the pillar edge length in Fig. 8*E*. The σ value is seen to increase slightly as the pillar size decreases from 20 μm to 10 μm and then increases more rapidly from 10 μm to 2 μm.

In contrast, no strain bursts were observed in L-beam torsion/bending across the entire specimen sizes tested, from *w* ~30 μm down to ~2 μm. An image of one deformed 2 μm L-beam is shown in Fig. 8*F*, the magnified image of the L-beam front surface, shown in the *Inset*, displays slip steps that are consistent with those shown in Fig. 2. Because of the existence of an elastic core in the torsion arm of the L-beams, dislocations nucleating from the specimen surfaces stay within the specimen volume and cannot escape from the opposite side of the specimen unimpeded. In uniaxial compression of micro- and nano-sized pillars,

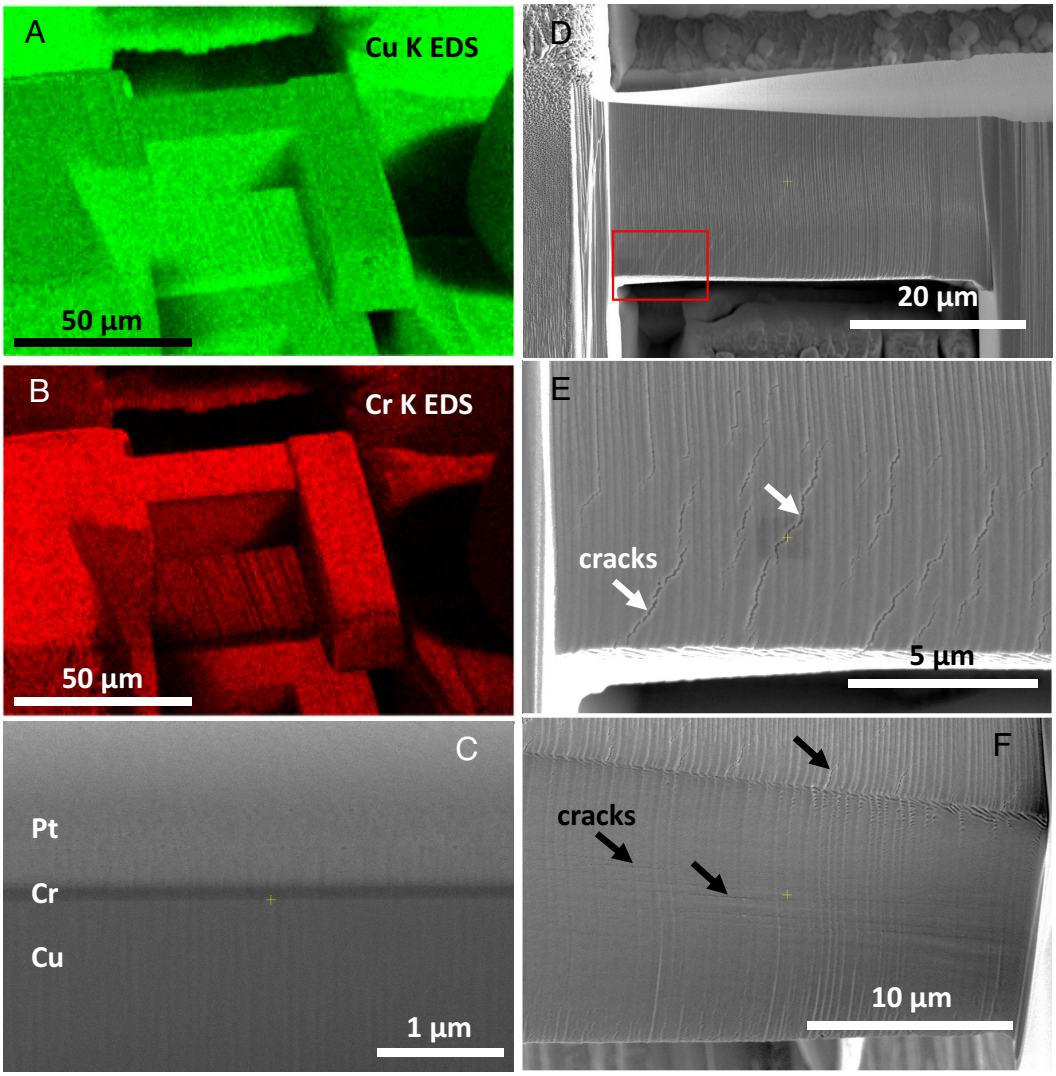

Fig. 5. <111> Cu L-beam surface passivation through deposition of a thin Cr coating: (*A* and *B*) Cu K and Cr K EDS maps of one Cu L-beam with w = 20 µm after deposition of a thin Cr coating layer; (*C*) a cross-section view of the Cr coating on the L-beam, the thickness of which is ~120 nm. The Pt layer was deposited onto the specimen prior to FIB milling for surface protection; (*D*) a low-magnification top view of a Cr-coated L-beam with w = 20 µm after deformation; (*E*) a higher magnification view of the L-beam top surface region outlined in the red square in (*D*); (*F*) a higher magnification view of the deformed L-beam front surface. Arrows in (*E* and *F*) highlight cracks in the Cr coating after deformation.

it is accepted that mechanisms governing dislocation production are responsible for the observed strength increase with decreasing specimen size (3). The strain bursts observed in such experiments result from motion of dislocations along a single slip plane across the entire specimen unimpeded (dislocation avalanche) and signify a lack of dislocation interactions, which is not the case for L-beam torsion. While effects of dislocation nucleation/production in the present L-beam experiments can be present, the interaction of dislocations contained within the deformed volume presents an additional physical element as compared to the case of uniaxial pillar compression. This dislocation interaction is what SGP attempts to model. The fact that the SGP FEM output largely matches the entire suite of the present L-beam experiments attests to the fidelity of the SGP model to the physics at hand. Whether combined torsion/bending of even smaller L-beams, e.g., with sizes in the nanoscale, can enter a regime where dislocation nucleation effects completely dominate the deformation behavior is an interesting question, one that is left for future studies.

One additional remark is made regarding the potential influence of ion beam damage of specimen surfaces on the present results. A recent comparative study on the use of Xe^+ PFIB and Ga^+ FIB for TEM specimen preparation showed that Xe incorporation in Al TEM specimens is less as compared to Ga incorporation and that Xe^+ PFIB produced a thinner amorphous layer, ~3 nm, in the final TEM specimen as compared to Ga^+ FIB (49). Another study on the use of Xe^+ PFIB showed that a ~30 nm thick amorphous layer was produced in Si by a Xe^+ ion beam at normal incidence, a smaller thickness as compared to what would be produced by a Ga^+ ion beam under comparable conditions (50). As previous studies on uniaxial compression of Au pillars fabricated by Ga^+ FIB concluded that the effect of Ga^+ ion beam was not a significant influencing factor for the observed size effect (51), we surmise that the effect of Xe^+ ion damage on the presently studied Cu L-beam specimens should not be significant, especially at the larger specimen sizes. Additional studies in the future are needed for confirmation.

Summary Remarks and Recommendations

The aim of this paper is twofold: 1) to generate experimental data on the elastic-plastic behavior of a prototypical metallic structural element over ranges of specimen sizes and plastic strains relevant

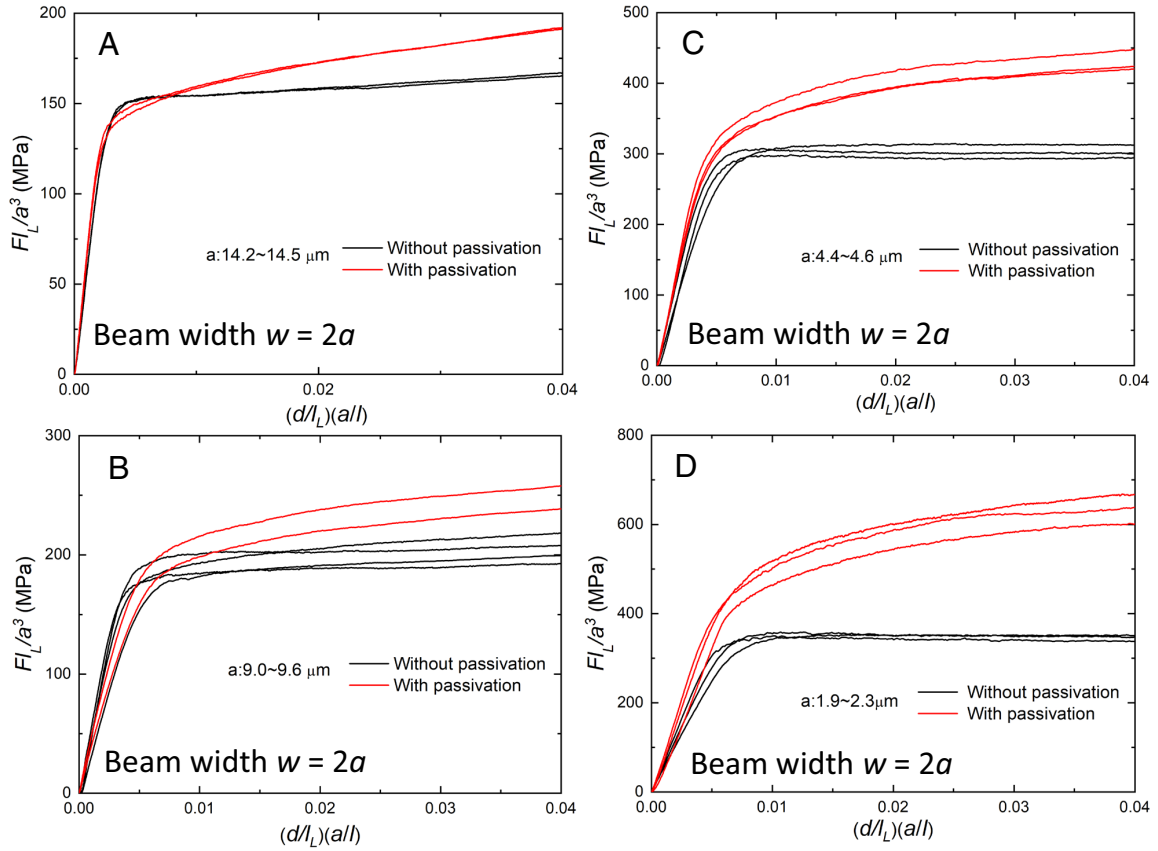

Fig. 6. Mechanical response of <111> Cu 2 × 4 L-beams with and without surface passivation: measured values of scaled torque Fl_L/a^3 vs. $(d/l_L)(a/l)$ for 2 × 4 L-beams with half-width a (*A*) ~14.3 μm; (*B*) ~9.3 μm; (*C*) ~4.5 μm; (*D*) ~2.1 μm. The black and red lines in (*A*–*D*) denote, respectively, measured response curves without and with surface passivation. Separate lines denote results from measurements on separate specimens.

to microscale applications and 2) to highlight some of the outstanding issues that must be addressed before basic SGP theories will be capable of predicting structural response for micron-scale applications with a degree of fidelity similar to that provided by conventional plasticity theory for large-scale applications.

Experiments have been performed on a single-crystal Cu L-beam structural element subject to combined torsion and bending. Loads have been increased to the point where plastic yielding of the structure occurs and then increased further into the range where plasticity dominantly governs the load-carrying capabilities and deflections. Specimens with a cross-sectional dimension ranging from 30 μm down to 2 μm have been tested, covering a range relevant to micron-scale applications, especially at sizes as small as 2 μm. The trend of higher effective yield strength with decreasing specimen size is similar to that seen in indentation testing of single crystals in the same size range (4, 52). The size-dependent strengthening effect is significant, with the yield strength of specimens with 2 μm cross-sections being ~three times of those with 30 μm cross-sections. In addition, we have performed experiments demonstrating the potential of surface passivation, achieved by a

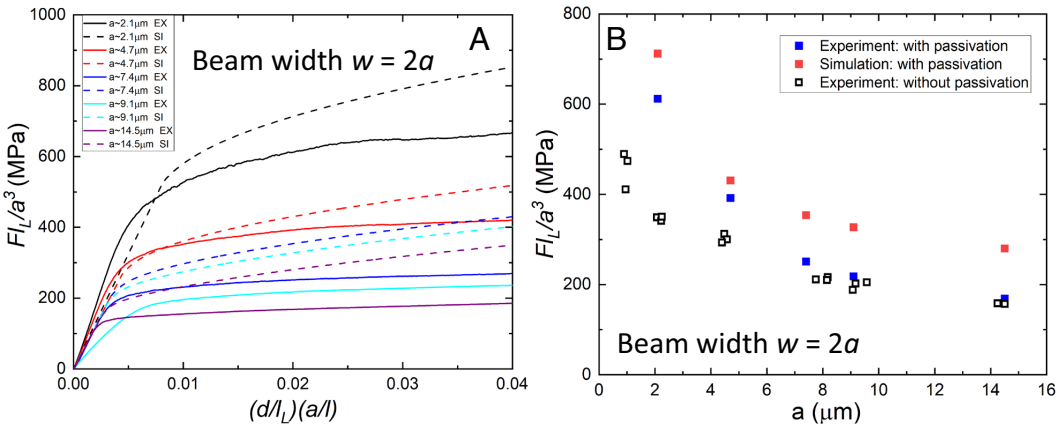

Fig. 7. Mechanical response of <111> Cu 2 × 4 L-beams with passivated surfaces: (*A*) experimental data (solid line) and FEM simulation output (dashed line) at different beam half-width a; (*B*) measurement and simulation values of Fl_L/a^3 at $(d/l_L)(a/l) = 0.02$ vs. a. The blue and red solid symbols in (*B*) denote, respectively, measurement and simulation values. For comparison, the open symbols in (*B*) plot the experimental values for 2 × 4 L-beam specimens with unpassivated surfaces.

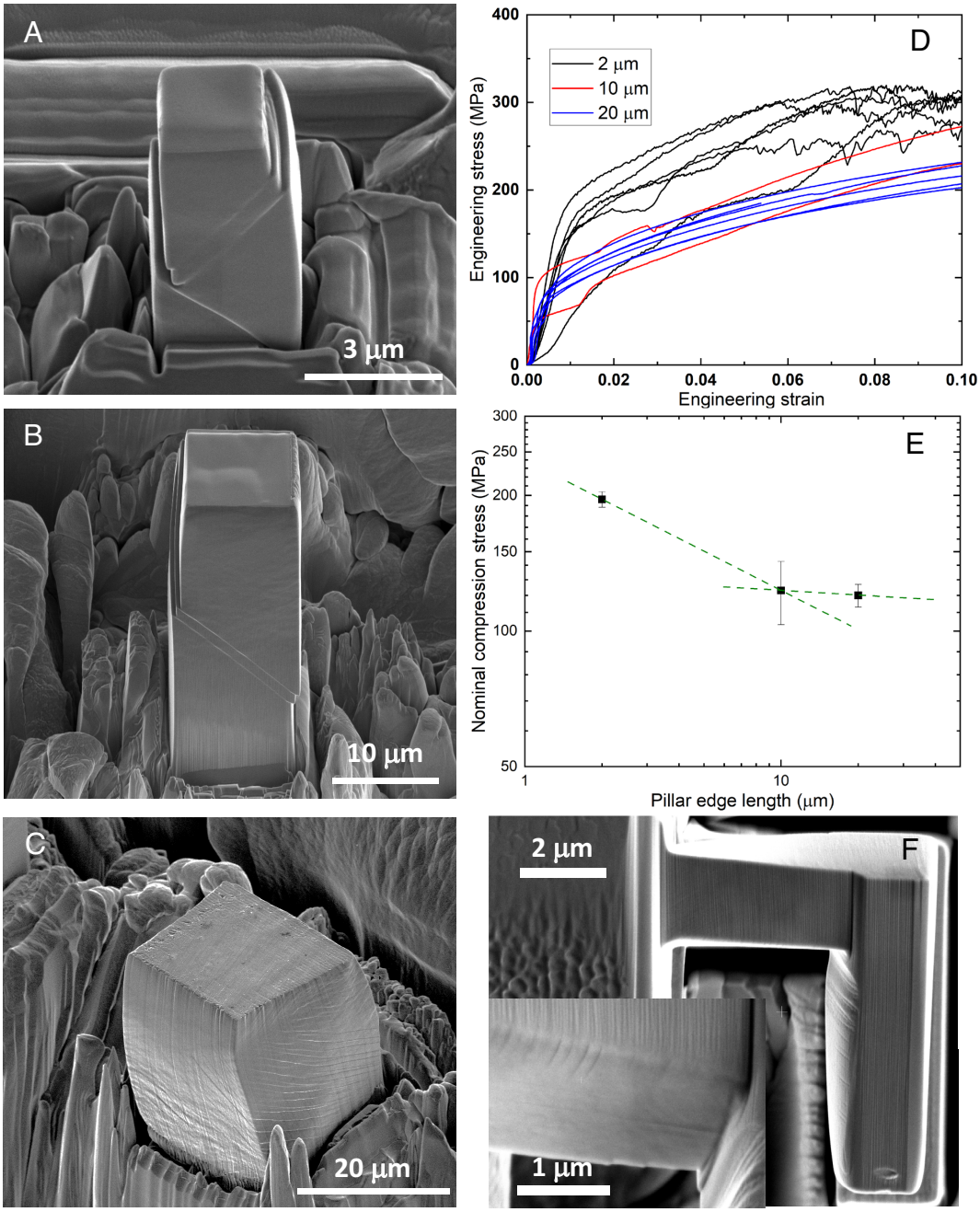

Fig. 8. Typical morphology after uniaxial compression of <001> Cu square pillars to an engineering strain $\varepsilon \sim 0.3$ at pillars dimensions of (*A*) 2 μm × 2 μm × 6 μm, (*B*) 10 μm × 10 μm × 30 μm, (*C*) 20 μm × 20 μm × 60 μm; (*D*) nominal engineering compression stress σ vs. ε for a number of 2 μm, 10 μm, and 20 μm <001> Cu pillars; (*E*) a log-log plot of σ at $\varepsilon = 0.02$ vs. the pillar edge length; (*F*) morphology of one deformed 2 μm L-beam. The green dashed lines in (*E*) are guides to the eye. The *Inset* in (*F*) shows the slip steps on the L-beam front surface.

thin Cr coating, for elevating the effective yield strength of the structural elements. This effect increases with decreasing specimen size, and for the smallest specimens tested, raising the apparent yield stress significantly beyond the value attained without surface passivation.

The potential for gradient plasticity effects employed in combination with surface passivation to strengthen microscale structures is most clearly illustrated by the L-beam specimen with a 4 μm cross-section in Fig. 7, whose yield strength is more than three times that of the 30 μm specimen. The strength magnification for a specimen with a 2-μm cross-section would have almost certainly been even higher had a passivated specimen been tested. The present set of experiments on the L-beam specimens systematically reveals the potential of very thin surface coatings to appreciably enhance the strength of micron-scale structures. However, we should call attention to an early experimental study by Vlassak et al. (53), which demonstrated that surface passivated Cu thin films in bending have higher strength than their unpassivated counterparts, and a very recent study by Xie et al. (54) on torsion of polycrystalline Cu wires with diameters ranging from 50 μm to 25 μm, which revealed a small, but clear, strengthening effect of a thin Ti surface coating.

Strain gradient hardening and dislocation blocking at the surface with a thin coating are major effects. To be useful as a design and analysis tool for structural applications in the micron range, a SGP theory must be able to replicate these effects with a level

of fidelity adequate for "engineering purposes." The expression engineering purposes is used here because all experienced structural practitioners will be well aware that characterizing plastic behavior is seldom straightforward and one can always find examples or applications that challenge any constitutive model, whether at large or small scales. The shortcomings of the SGP model employed in the present simulations, e.g., isotropic hardening rather than a single-crystal model, have been partly overcome by calibrating the strain hardening index, N, and the material length parameter, l_D, using selected deformation histories of the L-beam itself. The finite element simulations carried out in this paper captured the entire set of deformation histories of the two families of L-beams with reasonable accuracy, and, most significantly, they replicated the effect of surface passivation by requiring the plastic strain to vanish at the surface with no change in the material parameters, although there was some unsatisfactory discrepancy for the larger specimens. As emphasized in the paper, the size range of the L-beam specimens is substantial and covers much of the range relevant to micron-scale plasticity for structural applications.

The recommendations below focus on three open issues relevant to the further development of SGP, which we believe are among the most important for structural applications. The first is further work on employing surface modifications, e.g., the use of thin surface coatings, to limit plasticity at free surfaces as a mechanism to strengthen micron-scale structures. Efforts to exploit and model this effect are in their early stages. Further validation of the theory with definitive experiments, such as those in this paper, is required. A parallel effort is underway to align theory and experiment for plastically sheared metal layers with thicknesses in the micron range that are sandwiched between nondeforming substrates (55–58). The similarity between the two efforts stems from the fact that both require the characterization of the constraint on plasticity associated with dislocation blocking at an interface, while an important difference is that the experimental data for the shear layers have, at least until now, all been at large strains (of order unity and larger) while the emphasis in the present paper has been focused on plastic strains that can be large compared to elastic strains but still small compared to unity.

The second recommendation calls for more extensive computational/experimental studies to demonstrate the predictive capabilities of SGP for micron-scale structures. Specifically, a wider variety of deformation geometries and loading conditions representative of potential applications should be studied, as comparison between experimental results and simulation outcomes will serve to better calibrate/modify the SGP theory to deal with complex stress states. A wider array of examples is needed to establish the universality of the theory as well as its limits. We noted in this paper that a 3D small strain, finite element code formulated for single-crystal SGP was not available to analyze the L-beam specimens. The availability of such codes is essential if advances such as those suggested above are to occur and, indeed, for implementing SGP to design and analyze structures in micron-scale applications. This remark also applies to efforts on verifying, or indeed, establishing gradient hardening laws for single crystals, a subject largely unexplored experimentally, and on establishing a lower size limit for the applicability of continuum SGP formulations.

The last recommendation relates to the inadequacy mentioned in the paper of some of the most widely used SGP constitutive models, such as that used in this paper, in applications where distinctly nonproportional loading histories occur. Other constitutive models are available for both isotropic plasticity and single crystals (45, 46), which give identical, or closely similar, predictions to the class of models used in this paper when the loading is proportional or nearly proportional, and these alternative models do not give rise to physically unacceptable "elastic gaps" at load transitions. These alternative models have not been validated by experiments replicating representative nonproportional load transitions, which is essential if they are to be used with confidence for micron-scale applications.

Materials and Methods

Experimentation. Two series of L-beam specimens were machined from a disk-shaped, <111> oriented Cu single crystal (5 mm × 5 mm × 1 mm, MTI Corp.) using a Xe PFIB/scanning electron microscope instrument (PFIB/SEM, ThermoFisher Helios G4). A Xe^+ ion beam of 30 keV and 1 nA was used in the finish machining step for all L-beam surfaces. Scanning images and X-ray EDS maps of the external surfaces of as-machined, deformed, and Cr-coated specimens were acquired using the Helios G4 PFIB/SEM with X-ray energy-dispersive spectroscopy/electron backscatter diffraction attachments (EDS/EBSD, Oxford Instruments) and an ThermoFisher EasyLift® nanoprobe attachment for site-selective lift-out. Cr coating deposition onto the surface of L-beam specimens was carried out in a custom-built, high-vacuum vapor phase deposition system with a base pressure $<8 \times 10^{-9}$ Torr. Deposition occurred in pure Ar (99.999%) at a pressure of ~10 mTorr using two 7.5 cm diameter magnetron sputter sources (MeiVac MAK) with elemental Cr targets (Kurt Lesker, 99.9%).

Characterization of deformed specimens by TEM was conducted on a JEOL JEM-F200 field emission instrument operated at 200 keV. Electron transparent specimens were prepared from site-selective lift-out slices from deformed L-beam specimens in the longitudinal cross-section orientation, with further details described in *SI Appendix*, section S2. Micro/mesoscale torsion tests were conducted in-situ an FEI Quanta3D FEG Ga^+ FIB/SEM instrument using a nanomechanical testing system (FemtoTools NMT04). Compression loading of the L-beam specimens was conducted in a displacement-controlled mode, with the displacement rate ranging from 60 nm/s to 10 nm/s and the corresponding strain rate adjusted to be approximately a constant of $\sim 10^{-2}\,s^{-1}$.

SGP Theory and Numerical Modeling. The nonincremental gradient-enriched plasticity theory by Gudmundson (24) and Fleck and Willis (27, 28) is adopted to account for the L-beam experimental results. The theory constitutes a phenomenological extension of classical isotropic viscoplasticity, with only one additional material quantity being the dissipative material length parameter ℓ_D. In addition to ℓ_D, the plastic material response is controlled by a reference flow stress σ_Y, a strain hardening exponent N, an amplification factor k, a reference strain rate $\dot{\varepsilon}_0$, and a rate sensitivity exponent m. A classical power-law viscoplastic potential is employed, such that $\Phi = \sigma_F \frac{\dot{\varepsilon}_0}{m+1} \left(\dot{E}^p/\dot{\varepsilon}_0\right)^{m+1}$, whereby the effective stress is given by $\sigma_C = \sigma_F \left(\dot{E}^p/\dot{\varepsilon}_0\right)^m$. In uniaxial tension at $\dot{\varepsilon} = \dot{\varepsilon}_0$, the material obeys the power-law relation: $\sigma_F = \sigma_Y(1 + k\left(E^P\right)^N)$, with the gradient-enriched effective strain rate being $\dot{E}^p = \sqrt{\frac{2}{3}\dot{\varepsilon}^p_{ij}\dot{\varepsilon}^p_{ij} + \left(\ell_D\right)^2 \dot{\varepsilon}^p_{ij,k}\dot{\varepsilon}^p_{ij,k}}$. In this way, the conventional dissipation owing to storage and movement of statistically stored dislocations occurs through the plastic strains $\dot{\varepsilon}^p_{ij}$ while additional dissipation takes place due to GNDs required to accommodate plastic strain gradients $\dot{\varepsilon}^p_{ij,k}$ at the micron scale (19–21). The constitutive length parameter ℓ_D scales the contribution from gradient dissipation, with the conventional limit where the material response coincides with classical size-independent viscoplasticity attained for $\ell_D = 0$.

Using an updated Lagrangian approach, the gradient theory is built into a 3D FEM code accounting for finite strains and finite deformations. Following Nielsen and Niordson (43), the plastic strain rate field $\dot{\varepsilon}^p_{ij}$ and the displacement rate $\dot{u}_i$ are considered unknown field variables which are solved for in two successive steps. The 3D domain is discretized by two finite element meshes with an equal number of elements and coinciding corner nodes. Twenty-noded quadratic elements are used for the displacement field (nodal degrees of freedom are $\{\dot{u}_1, \dot{u}_2, \dot{u}_3\}$), and corresponding eight-noded linear elements are used for the plastic strain rate field (nodal degrees of freedom are $\{\dot{\varepsilon}^p_{11}, \dot{\varepsilon}^p_{22}, \dot{\varepsilon}^p_{12}, \dot{\varepsilon}^p_{13}, \dot{\varepsilon}^p_{23}\}$). The element-types are chosen to ensure compatibility between the total and plastic strain field, varying linearly within each element. A representative finite element mesh is shown in *SI Appendix*, section S3 and Fig. S2, with boundary conditions. As shown

in *SI Appendix*, Fig. S2, the L-beam is clamped at $x_1 = 0$ such that $u_i = 0$, while a tip load F is prescribed incrementally.

In contrast to classical plasticity, the gradient-enriched theory allows blocking of dislocation movement at a passivated surface by constraining the plastic flow. Thus, the gradient model can mimic the surface passivation imposed in the experiments by deposition of a thin Cr layer onto the specimen surfaces. This is done by enforcing $\dot{\varepsilon}^p_{ij} = 0$ on the top, front, and back surfaces of the L-beam specimen, in accordance with the present experiments. These alternative boundary conditions lead to steep gradients of plastic strain near the passivated surface which, in turn, requires a much finer mesh than would otherwise be required. We have systematically refined the FEM mesh in these regions to ensure that the response is mesh-independent.

Data, Materials, and Software Availability. All study data are included in the article and/or supporting information.

ACKNOWLEDGMENTS. B.Z. and W.J.M. acknowledge partial project support from the NSF EPSCoR program, under awards OIA-1541079, OIA-1946231, and OIA-2118756. Use of experimental facilities at the Louisiana State University Shared Instrumentation Facility, a part of the Louisiana Core User Facilities, is acknowledged. W.J.M. acknowledges the generous support of Dr. B. Lu for the microplasticity research. K.L.N. is financially supported by the Villum Foundation in the project "Micron-Scale Crashworthiness," grant No. 00028205. Technical assistance with TEM data acquisition by Dr. Andrew C. Meng and with Cr coating deposition by Dr. Xiaoman Zhang is acknowledged with thanks.

Author affiliations: [a]Department of Mechanical and Industrial Engineering, Louisiana State University, Baton Rouge, LA 70803; [b]Department of Civil and Mechanical Engineering, Section of Solid Mechanics, Technical University of Denmark, Copenhagen DK-2800, Denmark; and [c]School of Engineering and Applied Sciences, Materials Science and Mechanical Engineering, Harvard University, Cambridge, MA 02138

1. N. A. Fleck, G. M. Muller, M. F. Ashby, J. W. Hutchinson, Strain gradient plasticity - theory and experiment. *Acta Metall. Mater.* **42**, 475–487 (1994).
2. M. D. Uchic, D. M. Dimiduk, J. N. Florando, W. D. Nix, Sample dimensions influence strength and crystal plasticity. *Science* **305**, 986–989 (2004).
3. J. R. Greer, J. T. M. De Hosson, Plasticity in small-sized metallic systems: Intrinsic versus extrinsic size effect. *Prog. Mater. Sci.* **56**, 654–724 (2011).
4. Q. Ma, D. R. Clarke, Size-dependent hardness of silver single-crystals. *J. Mater. Res.* **10**, 853–863 (1995).
5. J. S. Stolken, A. G. Evans, A microbend test method for measuring the plasticity length scale. *Acta Mater.* **46**, 5109–5115 (1998).
6. K. Chen, W. J. Meng, F. H. Mei, J. Hiller, D. J. Miller, From micro- to nano-scale molding of metals: Size effect during molding of single crystal Al with rectangular strip punches. *Acta Mater.* **59**, 1112–1120 (2011).
7. B. Zhang *et al.*, Understanding of plasticity size-effect governed mechanical response and incomplete die filling in a microscale double-punch molding configuration. *Int. J. Mech. Sci.* **172**, 105406 (2020).
8. B. Zhang *et al.*, Grain-size affected mechanical response and deformation behavior in microscale reverse extrusion. *Materialia* **6**, 100272 (2019).
9. B. Zhang, A. C. Meng, W. J. Meng, Deviation of mechanical behavior in microforming from continuum scaling: A geometrically necessary dislocation storage perspective. *Int. J. Mach. Tool. Manuf.* **169**, 103795 (2021).
10. K. J. Juul, K. L. Nielsen, C. F. Niordson, Steady-state numerical modeling of size effects in micron scale wire drawing. *J. Manuf. Process.* **25**, 163–171 (2017).
11. K. L. Nielsen, C. F. Niordson, J. W. Hutchinson, Rolling at small scales. *J. Manuf. Sci. Eng-T ASME* **138**, 41004 (2016).
12. K. L. Nielsen, J. W. Hutchinson, Plastic buckling of columns at the micron scale. *Int. J. Solids Struct.* **257**, 111558 (2022).
13. L. J. Gibson, M. F. Ashby, *Cellular Solids* (Cambridge University Press, Cambridge, UK, ed. 2, 1997).
14. A. G. Evans, J. W. Hutchinson, M. F. Ashby, Cellular metals. *Curr. Opin. Solid. State Mater. Sci.* **3**, 288–303 (1998).
15. A. A. Zadpoor, Mechanical meta-materials. *Mater. Horiz.* **3**, 371–381 (2016).
16. C. X. Lu *et al.*, Architectural design and additive manufacturing of mechanical metamaterials: A review. *Engineering* **17**, 44–63 (2022).
17. T. A. Schaedler *et al.*, Ultralight metallic microlattices. *Science* **334**, 962–965 (2011).
18. R. K. Prusty *et al.*, Spherical indentation response of a Ni double gyroid nanolattice. *Scripta Mater.* **188**, 64–68 (2020).
19. J. F. Nye, Some geometrical relations in dislocated crystals. *Acta Metall.* **1**, 153–162 (1953).
20. M. F. Ashby, Deformation of plastically non-homogeneous materials. *Philos. Mag.* **21**, 399–424 (1970).
21. K. C. Russell, M. F. Ashby, Slip in aluminum crystals containing strong, plate-like particles. *Acta Metall.* **18**, 891–901 (1970).
22. E. C. Aifantis, On the microstructural origin of certain inelastic models. *J. Eng. Mater-T ASME* **106**, 326–330 (1984).
23. N. A. Fleck, J. W. Hutchinson, Strain gradient plasticity. *Adv. Appl. Mech.* **33**, 295–361 (1997).
24. P. Gudmundson, A unified treatment of strain gradient plasticity. *J. Mech. Phys. Solids* **52**, 1379–1406 (2004).
25. M. E. Gurtin, L. Anand, A theory of strain-gradient plasticity for isotropic, plastically irrotational materials. Part I: Small deformations. *J. Mech. Phys. Solids* **53**, 1624–1649 (2005).
26. M. E. Gurtin, L. Anand, A theory of strain-gradient plasticity for isotropic, plastically irrotational materials. Part II: Finite deformations. *Int. J. Plasticity* **21**, 2297–2318 (2005).
27. N. A. Fleck, J. R. Willis, A mathematical basis for strain-gradient plasticity theory-Part I: Scalar plastic multiplier. *J. Mech. Phys. Solids* **57**, 161–177 (2009).
28. N. A. Fleck, J. R. Willis, A mathematical basis for strain-gradient plasticity theory. Part II: Tensorial plastic multiplier. *J. Mech. Phys. Solids* **57**, 1045–1057 (2009).
29. H. Gao, Y. Huang, W. D. Nix, J. W. Hutchinson, Mechanism-based strain gradient plasticity - I. Theory. *J. Mech. Phys. Solids* **47**, 1239–1263 (1999).
30. Y. Huang, H. Gao, W. D. Nix, J. W. Hutchinson, Mechanism-based strain gradient plasticity - II. Analysis. *J. Mech. Phys. Solids* **48**, 99–128 (2000).
31. M. E. Gurtin, A gradient theory of single-crystal viscoplasticity that accounts for geometrically necessary dislocations. *J. Mech. Phys. Solids* **50**, 5–32 (2002).
32. G. Z. Voyiadjis, Y. Song, Strain gradient continuum plasticity theories: Theoretical, numerical and experimental investigations. *Int. J. Plasticity* **121**, 21–75 (2019).
33. C. F. O. Dahlberg, M. Boasen, Evolution of the length scale in strain gradient plasticity. *Int. J. Plasticity* **112**, 220–241 (2019).
34. Z. P. Gan, Y. M. He, D. B. Liu, B. Zhang, L. Shen, Hall-Petch effect and strain gradient effect in the torsion of thin gold wires. *Scripta. Mater.* **87**, 41–44 (2014).
35. D. J. Dunstan *et al.*, Elastic limit and strain hardening of thin wires in torsion. *Phys. Rev. Lett.* **103**, 155501 (2009).
36. A. J. Bushby, D. J. Dunstan, Size effects in yield and plasticity under uniaxial and non-uniform loading: Experiment and theory. *Philos. Mag.* **91**, 1037–1049 (2011).
37. D. B. Liu *et al.*, Size effects in the torsion of microscale copper wires: Experiment and analysis. *Scripta. Mater.* **66**, 406–409 (2012).
38. D. B. Liu *et al.*, Toward a further understanding of size effects in the torsion of thin metal wires: An experimental and theoretical assessment. *Int. J. Plasticity* **41**, 30–52 (2013).
39. W. Y. Lu, B. Song, Quasi-static torsion characterization of micro-diameter copper wires. *Exp. Mech.* **51**, 729–737 (2011).
40. G. M. Pharr, E. G. Herbert, Y. F. Gao, The indentation size effect: A critical examination of experimental observations and mechanistic interpretations. *Annu. Rev. Mater. Res.* **40**, 271–292 (2010).
41. M. Walter, O. Kraft, A new method to measure torsion moments on small-scaled specimens. *Rev. Sci. Instrum.* **82**, 35109 (2011).
42. S. P. Timoshenko, J. N. Goodier, *Theory of Elasticity* (McGraw-Hill, New York, ed. 3, 1987).
43. K. L. Nielsen, C. F. Niordson, A finite strain FE-Implementation of the Fleck-Willis gradient theory: Rate independent versus visco-plastic formulation. *Eur. J. Mech a-Solid* **75**, 389–398 (2019).
44. N. A. Fleck, J. W. Hutchinson, J. R. Willis, Strain gradient plasticity under non-proportional loading. *Proc. R. Soc. A-Math. Phys.* **470**, 20140267 (2014).
45. N. A. Fleck, J. W. Hutchinson, J. R. Willis, Guidelines for constructing strain gradient plasticity theories. *J. Appl. Mech-T ASME* **82**, 071002 (2015).
46. C. Nellemann, C. F. Niordson, K. L. Nielsen, An incremental flow theory for crystal plasticity incorporating strain gradient effects. *Int. J. Solids Struct.* **110**, 239–250 (2017).
47. M. R. Stoudt, R. E. Ricker, R. C. Cammarata, The influence of a multilayered metallic coating on fatigue crack nucleation. *Int. J. Fatigue* **23**, S215–S223 (2001).
48. B. Zhang *et al.*, On the failure mechanisms of Cr-coated 316 stainless steel in bending fatigue tests. *Int. J. Fatigue* **139**, 105733 (2020).
49. X. Zhong *et al.*, Comparing Xe+ pFIB and Ga+ FIB for TEM sample preparation of Al alloys: Minimising FIB-induced artefacts. *J. Microscopy* **282**, 101–112 (2021).
50. L. A. Giannuzzi, N. S. Smith, TEM specimen preparation with plasma FIB Xe+ ions. *Microsc. Microanal.* **17**, 646–647 (2011).
51. J. R. Greer, W. D. Nix, Nanoscale gold pillars strengthened through dislocation starvation. *Phys. Rev. B* **73**, 245410 (2006).
52. W. D. Nix, H. J. Gao, Indentation size effects in crystalline materials: A law for strain gradient plasticity. *J. Mech. Phys. Solids* **46**, 411–425 (1998).
53. Y. Xiang, J. J. Vlassak, Bauschinger and size effects in thin-film plasticity. *Acta Mater.* **54**, 5449–5460 (2006).
54. Y. Y. Xie *et al.*, Size and passivation effects in the torsion of thin metallic wires. *Acta Mech. Sinica.* **39**, 422346 (2023).
55. Y. Mu, J. W. Hutchinson, W. Meng, Micro-pillar measurements of plasticity in confined Cu thin films. *Extreme Mech. Lett.* **1**, 62–69 (2014).
56. X. Zhang *et al.*, Mechanical failure of metal/ceramic interfacial regions under shear loading. *Acta Mater.* **138**, 224–236 (2017).
57. C. F. O. Dahlberg, M. Ortiz, Fractional strain-gradient plasticity. *Eur. J. Mech. a-Solid.* **75**, 348–354 (2019).
58. M. Kuroda, A. Needleman, A simple model for size effects in constrained shear. *Extreme Mech. Lett.* **33**, 100581 (2019).

PNAS

Supporting Information for

Towards the development of plasticity theories for application to small scale metal structures

Bin Zhang[1], K.L. Nielsen[2], J.W. Hutchinson[3], W.J. Meng[1]

[1]Department of Mechanical and Industrial Engineering, Louisiana State University, Baton Rouge, Louisiana 70803, U.S.A.

[2]Department of Civil and Mechanical Engineering, Section of Solid Mechanics, Technical University of Denmark, DK-2800 Kgs. Lyngby, Denmark

Corresponding authors: J.W. Hutchinson, W.J. Meng
Email: jhutchin@fas.harvard.edu; wmeng1@lsu.edu

This PDF file includes:

Supporting text
Legends for Movie S1
Figures S1 to S2
Legends for Datasets S1, S2, and S3

Other supporting materials for this manuscript include the following:

Movies S1
Datasets S1, S2, and S3

SI Section S1. Video recording of a typical L-beam deformation process

Movie S1 (SI L-beam compression video.avi, in a separate file) documents the deformation process of one <111> Cu L-beam specimen, with a width w ~20 μm, in-situ an FEI Quanta3D FEG Ga^+ FIB/SEM instrument. The duration of the entire loading process was ~427 sec. The video playback has been speeded up by about a factor of 20. The extensive torsional deformation of the torsion arm of the L-beam specimen is evident from the video. Similar deformation morphologies are observed in all L-beam torsion/bending experiments.

SI Section S2. Fabrication of longitudinal cross section TEM lamella of deformed L-beam specimens

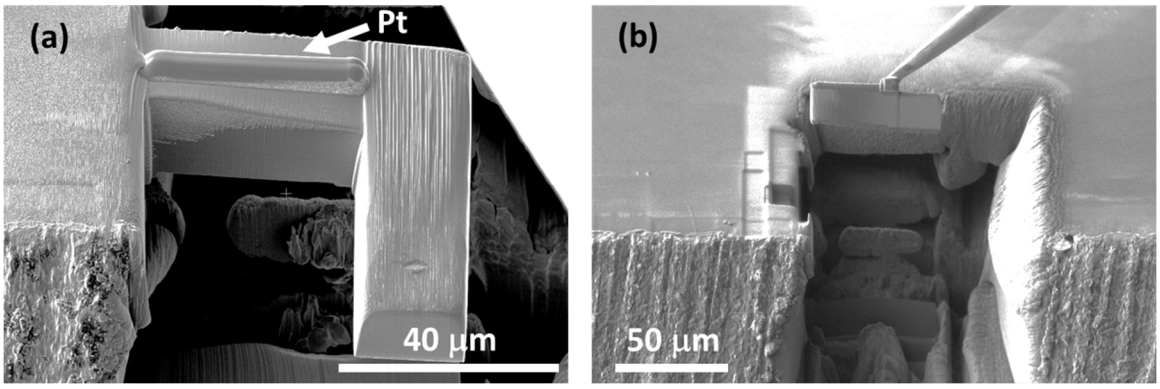

Fig. S.1. Fabrication of longitudinal cross section TEM lamella from deformed L-beam specimens.

Figure S.1(a) shows a tilted-view SEM image of one deformed <111> Cu L-beam specimen with a Pt strip deposited along the middle part of the top surface of the torsion arm through Xe^+ focused ion beam catalyzed deposition, for the purpose of specimen protection in the subsequent ion beam milling process.

After Pt deposition, the load arm portion of the L-beam specimen was first removed by focused ion beam milling in the ThermoFisher Helios™ G4 Xe^+ plasma focused ion beam/scanning electron microscope (PFIB/SEM) instrument at a Xe^+ ion beam voltage of 30kV. Additional FIB milling from the front and back sides of the L-beam torsion arm was then performed to isolate the material slice underneath the Pt strip. The PFIB instrument houses a precision nanoprobe for specimen attachment and lift-out (ThermoFisher EasyLift™). Standard procedures for specimen slice definition, probe attachment, and lift-out were followed.

Figure S.1(b) shows the longitudinal specimen slice attached to the nanoprobe. The lift-out slice was attached to a TEM grid and thinned in the PFIB instrument. The Xe^+ ion beam voltage used for final lamella thinning was 8 kV. It is noted that the lift-out specimen slice and the consequent TEM lamella are parallel to the front surface of the L-beam torsion arm.

SI Section S3. Strain gradient plasticity finite element method simulations

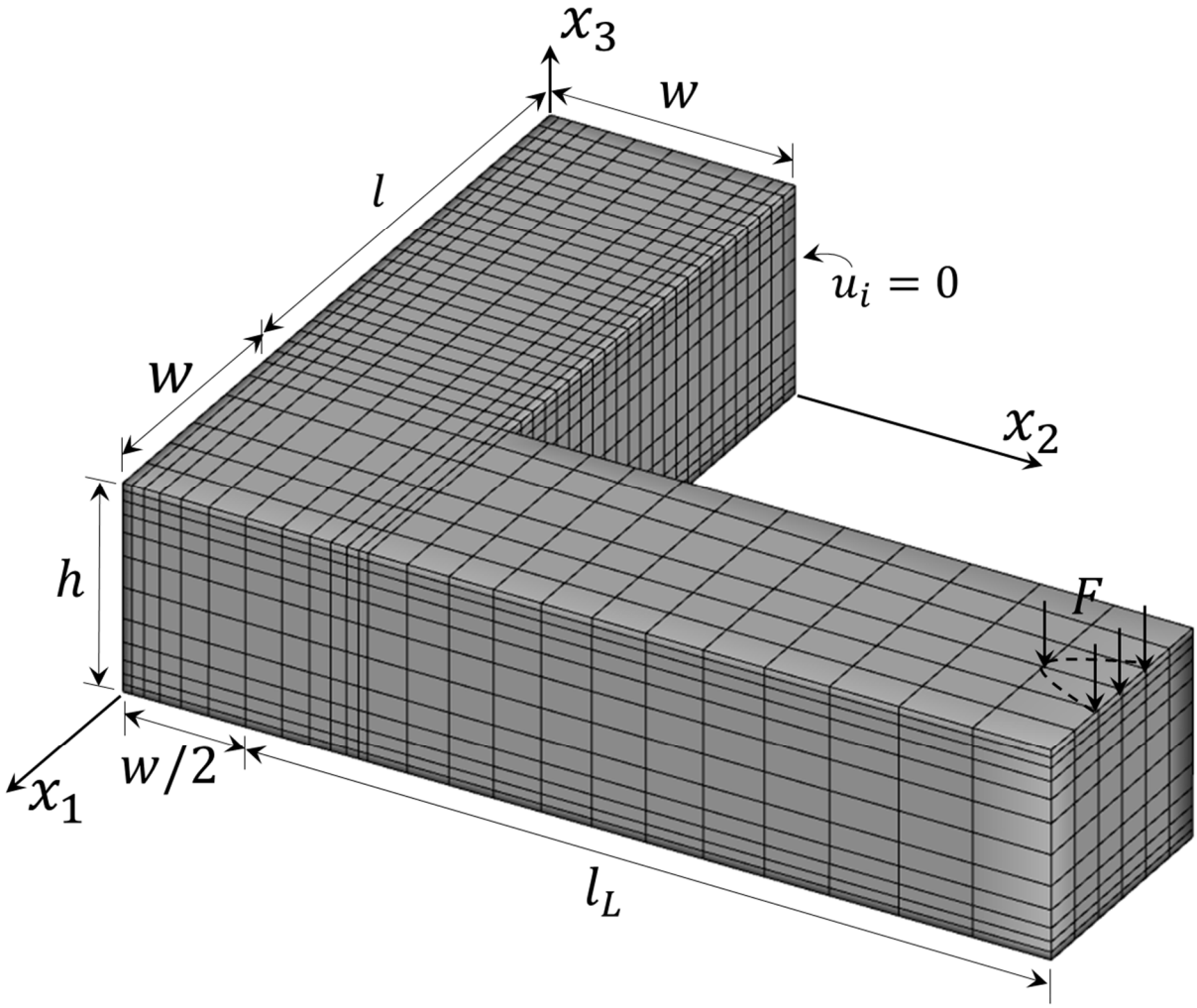

Fig. S.2. Representative finite element mesh and parametrization used in the 3D SGP FEM simulations. The L-beam is clamped at $x_1 = 0$ such that $u_i = 0$ and loaded by a tip force F in a circular region to mimic the punch. Additional descriptions are given in the Section "Materials and methods" of the main text. The material parameters used in the simulations are given in Table 1 of the main text.

The L-beam test setup is modeled using the finite element method (FEM). **Figure S.2** shows a representative mesh with the L-beam discretized by twenty-node and eight-node iso-parametric elements for the displacement and plastic strain rate fields, respectively. The element density is concentrated in the torsion arm of the L-beam and gradually made coarser in the load arm, primarily subjected to elastic bending. Moreover, the mesh is graduated from the center towards the surface of the torsion arm in order to accommodate the plastic strain gradients. This mesh graduation is particularly important when

introducing surface passivation, as additional plastic strain gradients develop in the L-beam near the constrained surfaces. The two surface conditions considered experimentally are modeled by imposing i) traction-free surfaces (both conventional $T_i = 0$ and higher order $\tau_{ij} = 0$ tractions) for the unpassivated L-beams, and ii) constrained plastic flow at the top and side surfaces with $\varepsilon_{ij}^{p} = 0$ for the surface passivated L-beams. In the latter case, the bottom surface is kept traction free to mimic the passivation layer deposited by vapor phase deposition. Additional descriptions are given in the Section "Effects of surface passivation" of the main text.

All beams are considered rigidly supported at the root of the L-beam such that $u_i = 0$ at $x_1 = 0$ and an incremental load F is applied at the tip of the load arm, according to the experimental procedure. Moreover, individual dimensions for each L-beam are considered (taking the average of each L-beam size) in order to better align the model results with the experiments.

SI Section S4. Measured data on L-beam deformation

A select number of raw force-displacement data curves together with the processed data curve, scaled in the manner as described in Eq. (1) of the main text, are documented in Microsoft EXCEL datasheet format. The associated specimen dimensions are also provided. The names of dataset files are listed below:

Dataset S1: (2×4 unpassivated L beam raw data and scaled data.xlsx, in a separate file) This dataset contains raw and processed data obtained from deformation of six unpassivated 2×4 L-beams. The actual dimensions of each L-beam specimen are given in the file.

Dataset S2: (2×4 passivated L beam raw data and scaled data.xlsx, in a separate file) This dataset contains raw and processed data obtained from deformation of five passivated 2×4 L-beams. The actual dimensions of each L-beam specimen are given in the file.

Dataset S3: (2×6 unpassivated L beam raw data and scaled data.xlsx, in a separate file) This dataset contains raw and processed data obtained from deformation of five unpassivated 2×6 L-beams. The actual dimensions of each L-beam specimen are given in the file.

All three EXCEL files are password protected to ensure no alterations to the entries. This security measure will not impede researchers' access to the data.